# Electronic correlation effects on the neutralization of $Ga^+$ scattered by a gold surface

M. S. Tacca,[1] F. Bonetto,[1,2,*] and E. C. Goldberg[1,2]

[1]*Instituto de Física del Litoral (CONICET-UNL), Güemes 3450, S3000GLN Santa Fe, Argentina*

[2]*Departamento de Materiales, Facultad de Ing. Química, Universidad Nacional del Litoral, Santiago del Estero 2829, S3000AOM Santa Fe, Argentina*

(Received 5 May 2017; revised manuscript received 3 July 2017; published 17 August 2017)

The monotonous increasing with temperature behavior of the neutralization of $Ga^+$ scattered by a gold surface plus the nonmagnetic character of the ion induced to disregard the important electronic correlation effects. In this work, we show that contrary to this assumption, the electron-electron interaction in the Ga site is crucial for describing the experimental results. We extend the formalism previously used in the $Sr^+$/Au system to include more than one valence orbital in the projectile, which is the case of $Ga^+$, where the neutralization occurs to a *p*-type shell. We consider the six possible orbital-spin neutral configurations in a correlated way within the Anderson model. The comparison with the results obtained from a noninteracting electron model allows one to infer how important the many-body effects in the charge exchange between $Ga^+$ and the gold surface are. We also found that the proximity of the projectile one-electron energy levels to the substrate Fermi level determines the influence of electronic correlation effects on the neutral fraction and its temperature and velocity dependences.

DOI: 10.1103/PhysRevB.96.075424

## I. INTRODUCTION

It has been invoked that by carefully choosing the projectile-target combination in low-energy scattering experiments, the correlated behavior of electrons can be determined [1–8]. In Ref. [1], the temperature and ion velocity dependences of the neutral fraction of hyperthermal energy $Na^+$ ions scattered by a Cu(001) surface were experimentally studied, and theoretically described using a noninteracting Anderson model, while in Refs. [4,5], the neutral fraction of 2 keV $Ga^+$, $Mg^+$, and $Sr^+$ ions scattered by a polycrystalline Au surface was measured as a function of the substrate temperature. $Mg^+$/Au and $Sr^+$/Au systems have already been theoretically studied [9–11]. In Ref. [11], a very good agreement with the experimental results was obtained for the neutralization of $Mg^+$ on Au, and also in the case of $Sr^+$ on Au if a very slight temperature dependence of the substrate work function is assumed. On the other hand, the temperature dependence of the neutral fraction of $Ga^+$ scattered by a gold surface still lacks a proper theoretical description.

The effect of many-body interactions in any dynamical physical process is not straightforward. The first improvement over the noninteracting Anderson model in the case of neutral atoms with either one valence electron (Ga, Na, and so on) or two in a closed s-shell (Sr, Mg, He, and so on) consists of including the spin-fluctuation statistic, that is, the infinite correlation limit of the Anderson model. In the first case, we have the charge fluctuation $|00\rangle \leftrightarrow |\uparrow 0\rangle ; |0 \downarrow\rangle$ and, due to the spin degeneration, there are two possibilities of electron capture against only one in the loss process. In the second case, the charge fluctuation $|\uparrow\downarrow\rangle \leftrightarrow |\uparrow 0\rangle ; |0 \downarrow\rangle$ indicates that the electron loss has two possibilities, while the capture has only one. These unbalanced capture and loss processes introduce an important difference with respect to the noninteracting model, but the effect is negligible if the ionization energy is well defined either above or below the Fermi energy. For instance, in the neutralization of $He^+$ to its ground state, it is not expected that the spin-fluctuation statistic has an important effect since its large ionization energy makes the electron-loss processes unviable [12–16]. Then, we can infer that the strong electron-electron interaction in the localized projectile site will introduce appreciable effects when the projectile energy level is close to the Fermi level. The cases of Sr and Ga interacting with a gold surface and Na scattered by a Cu surface are good examples, at least far from the surface where the energy level is only shifted by the image potential. The shift of the projectile level caused by the short-range chemical interactions at closer distances from the surface may change this scenario.

In stationary processes, different regimes in the infinite correlation limit are identified depending on the relation between the atom energy level $\epsilon_\alpha$ (the Fermi level defines the zero energy) and its width $\Gamma$ due to the interaction with the band states [17,18]. The Kondo regime is reached when $\epsilon_\alpha/\Gamma < -1$, the mixed-valence regime when $-1 < \epsilon_\alpha/\Gamma < 1$, and the empty orbital regime when $\epsilon_\alpha/\Gamma > 1$. In the Kondo regime, the valence occupation decreases with the temperature, while an increasing occupation with temperature is characteristic of the empty orbital regime. Both temperature dependences can occur in the mixed-valence regime, depending on whether this regime is evolving from a Kondo or to an empty orbital regime. Therefore, along the projectile trajectory, the ion energy-level position relative to the target Fermi level and the projectile-surface interaction lead to different correlation regimes which will fade away when the projectile is moving with a finite velocity. It is well known that at low velocities, the loss of memory of the charge state during the trajectory is more pronounced. Then, the charge state of the projectile atom is defined far from the surface at the exit trajectory [2,19–21]. Therefore, a better-defined correlation regime is expected in this case, associated with the effective range of distances of charge definition, determining the temperature behavior of the neutral fraction. In the case of $Sr^+$ scattered by an Au surface [11], a Kondo regime is found in the ion-surface range of distances where the final charge state of

*bonetto@santafe-conicet.gov.ar

 

the projectile is defined. In this case and within the appropriate hole-picture description, an increase of the valence occupation (a decrease of the hole-state occupation) with temperature is found, as expected in the Kondo regime. Then, it is not necessary to expect a nonmonotonous temperature dependence of the neutral fraction for inferring electron correlations; and neither is it necessary to disregard possible correlated electron behavior in the case of $Ga^+$ because of the nonmagnetic character of the ion [4].

To assess the relevance of electron correlation effects, we have to compare the results obtained with a model that includes them with the corresponding results by using a noninteracting electron model. The comparison with the experimental data tells us whether or not the theoretical description of the electron-electron interaction is applicable.

In this paper, we focus on the scattering of $Ga^+$ by a polycrystalline Au surface. By taking into account the ionization level of Ga (−5.99 eV) compared with the Au work function (5.1 eV), the resonant process constitutes the main mechanism of neutralization. The charge fluctuation $Ga^+(4s^24p^0)$ to $Ga^0(4s^24p^1)$ involves, besides the spin-fluctuation statistic, the possibility of three different $p$-orbital configurations. The three $p$ orbitals are degenerated far from the surface, but at closer distances this degeneracy is lifted due to the ion-surface interaction. Then, we consider six orbital-spin configurations for the neutral Ga, i.e., $|\alpha_\sigma\rangle$ with $\alpha = x,y,z$, corresponding to the three $p_\alpha$ orbitals and $\sigma = \uparrow, \downarrow$, and describe the interacting system by using an Anderson Hamiltonian projected over the selected atom configuration space. The bond-pair model [22], proven to be a robust model to properly describe many interacting atom-surface systems [15,23–25], is used for calculating the Hamiltonian terms.

The correlation in nonequilibrium processes has also been described by using physical operators in the mixed boson-electron space, where the time-dependent Green functions appropriate for calculating the atom charge state probability are calculated by using either the noncrossing approximation (NCA) [6,7] or the equation-of-motion (EOM) method [26]. It was found that the semiclassical approximation leads to the same rate equations in both calculations, although a better description of the scattering dynamic process at low projectile velocity of an exactly solvable model was obtained for the EOM method, mainly in the Kondo and empty orbital regime [26]. Here we use the operator projection technique because it provides a straightforward description when many orbitals in the atom are included, and calculate the time-dependent Green functions by using the EOM method closed up to a second order in the coupling term [26].

Three different calculations are performed related to the treatment of electron correlation: the noninteracting electron model, an approximation including the spin fluctuations for the three $p$ orbitals treated independently, and the more complete calculation that includes the six orbital-spin neutral configurations treated in a correlated way. We find that neither the magnitude nor the temperature dependence of the measured neutral fraction [4] can be described by the noninteracting electron model. We show that including all the orbital-spin configurations as possible neutralization channels is essential for a proper description of the neutralization of $Ga^+$ in the scattering by an Au surface.

## II. THEORETICAL ASPECTS

### A. Atom charge state configurations and model Hamiltonian

The configurations of the projectile atom to be considered in the charge exchange process are determined from the relative position of the associated one-electron levels to the Fermi energy of the surface ($E_F$). For a $Ga^+$ ion, the neutralization to $Ga^0$ involves the ionization level (−5.99 eV), while in the $Ga^-$ formation from $Ga^0$, the affinity level becomes active (−0.31 eV). Given that the work function of a polycrystalline Au surface is 5.1 eV, we can state that $Ga^+ \leftrightarrow Ga^0$ will be the most probable charge exchange process.

The energy of the active one-electron levels of Ga varies with the normal distance of the atom from the surface ($z$), as it can be observed in Fig. 1. In this figure, the following one-electron levels are shown: those associated to the neutralization to $Ga^0(4p_x)$, $Ga^0(4p_y)$, or $Ga^0(4p_z)$; and the lowest-energy levels, in accordance with the Hund's rule, for the second electron in the transition from $Ga^0(4p^1)$ to $Ga^-(4p^2)$. We can observe that near the surface, the degeneracy of the $p$ orbitals is lifted into the two degenerated $p_x$ and $p_y$ orbitals parallel to the surface, and the $p_z$ orbital normal to the surface. Whenever results for the $p_x$ state are presented, it is implicit that the ones for the $p_y$ orbital are equivalent.

The short-range contributions to the energy levels shown in Fig. 1 are calculated by using the bond-pair model [22], which is based on a mean-field approximation and a symmetrically orthonormalized atomic basis set in the dimeric projectile-solid atom space. The energy-level shifts shown in Fig. 1 are due to the overlap and the electrostatic interactions, and they are calculated without allowing charge exchange between the atom and the surface [22]. The rather large range of influence of the interaction, up to about 7 a.u., is due to the the spatial extent of the atomic orbitals. As typical for metal surfaces, the long-range contribution is provided by a classical image potential. Particularly, we include an image potential that matches short-range interactions at an ion-surface distance of 8 a.u., with the

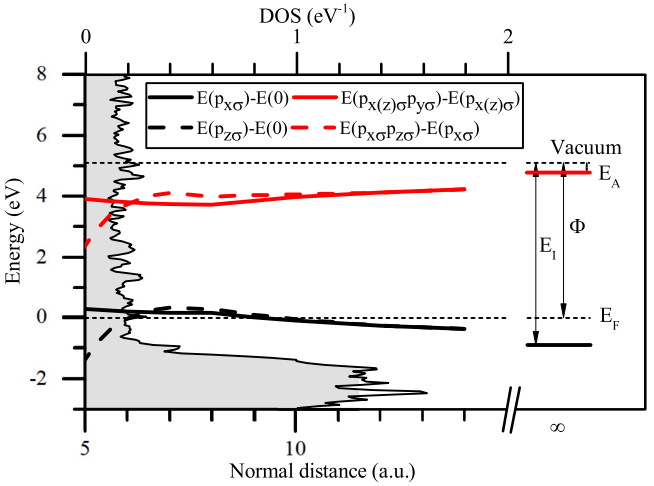


FIG. 1. One-electron energy levels defined as the difference between total energies. The Fermi energy is chosen as the zero energy. The ionization potential $E_I$, Au work function Φ, and electron affinity energy $E_A$ are indicated for comparison (right side). The Au(100) total DOS is also shown (shaded area).

image plane positioned at 1.6 a.u. from the surface [11]. The atomic states of Ga and Au are described by the Gaussian basis of Huzinaga [27,28], and the GAUSSIAN98 code [29] is used for calculating the one- and two-electron integrals required by the bond-pair model [22].

The position of the $Ga^-$ levels relative to the Fermi energy allows us to infer that the most probable charge configurations of Ga interacting with a gold surface are as follows:

(i) $|0\rangle$: zero electrons in the $4p$ shell, that is, $Ga^+$, and

(ii) $|\alpha_\sigma\rangle$: one electron in the $4p_\alpha$ orbital ($\alpha = x,y,z$) with spin $\sigma = \uparrow$ or $\downarrow$, that is, the ground state of neutral $Ga^0$.

To disregard the negative charge configurations means an infinite-U approximation. In this case, the restricted space of configurations is normalized according to

$$\sum_{\alpha,\sigma} |\alpha_\sigma\rangle \langle\alpha_\sigma| + |0\rangle \langle 0| = 1. \tag{1}$$

By projecting the Anderson Hamiltonian over the selected space of configurations, we arrive at the following expression:

$$\hat{H} = \sum_{\mathbf{k},\sigma} \epsilon_{\mathbf{k}} \hat{n}_{\mathbf{k}\sigma} + \sum_{\alpha,\sigma} E_\alpha |\alpha_\sigma\rangle \langle\alpha_\sigma| + E_0 |0\rangle \langle 0| + \sum_{\mathbf{k},\alpha,\sigma} (V_{\mathbf{k}\alpha} \hat{c}^\dagger_{\mathbf{k}\sigma} |0\rangle \langle\alpha_\sigma| + V_{\alpha\mathbf{k}} |\alpha_\sigma\rangle \langle 0| \hat{c}_{\mathbf{k}\sigma}). \tag{2}$$

In Eq. (2), the $\alpha$ ($\mathbf{k}$) index corresponds to the atom (solid band) states, $E_\alpha$ denotes the total energy of the $|\alpha_\sigma\rangle$ configuration, while the coupling term $V_{\alpha\mathbf{k}}$ corresponds to the hopping integral between the $p_\alpha$ orbital of the Ga atom and the $\mathbf{k}$-band state of the Au surface. These parameters depend on the position of the atom with respect to the surface, $\mathbf{R}$, which in turn depends on time in the ion-surface collision process through the ion velocity $\mathbf{v}$. The energy differences $E_\alpha - E_0$ define the one-electron levels $\epsilon_\alpha$, which tend to the ionization energy at infinite distance from the surface (see Fig. 1).

The more complete calculation consistent with the Hamiltonian (2) involves a correlated treatment of the six $|\alpha_\sigma\rangle$ atomic configurations. Nevertheless, as one of the main aims of the present paper is to determine the influence of the electron-electron interaction in the final charge state of the Ga atom, we perform three different calculations, in increasing order of complexity:

(i) Spinless (sl): Completely noninteracting spinless calculation, in which the electron spin is neglected and the different $p$-orbital configurations are treated independently.

(ii) Independent states (is): the different $p$-orbital configurations are treated independently, but the individual spin statistic is included.

(iii) Correlated states (cs): the six $|\alpha_\sigma\rangle$ atomic configurations are treated together in a correlated way and considering spin.

The comparative study of these three different approximations will provide information on how important the role of the electronic correlation is in this interacting system.

The average occupation number, $\langle \hat{n}_{\alpha_\sigma} \rangle = \langle |\alpha_\sigma\rangle \langle\alpha_\sigma| \rangle$, gives the probability of occurrence of the corresponding configuration. The spin index is omitted in the spinless case and, since the solid is nonmagnetic, there is spin degeneracy in the other two cases ($\langle \hat{n}_{\alpha_\sigma} \rangle = \langle \hat{n}_{\alpha_{\bar{\sigma}}} \rangle$). In the next section, we present the details of the calculation of $\langle \hat{n}_{\alpha_\sigma} \rangle$ in two different situations: the dynamic scattering process and the stationary situation of equilibrium.

### B. Dynamic and stationary situations

#### 1. Dynamic

The ion scattering by a surface is an out-of-equilibrium process. The occupation probability numbers are calculated by using the method of equations of motion (EOM) [30], based on the time evolution of Heisenberg operators. After some algebra, we obtain, for the correlated states approximation,

$$\frac{d \langle |\alpha_\sigma\rangle \langle\alpha_\sigma| \rangle}{dt} = \mathrm{Im} \left\{ \sum_{\beta,\mathbf{k}} V_{\alpha\mathbf{k}}(t) \int_{t_0}^{t} d\tau\, V_{\mathbf{k}\beta}(\tau) \left[ (2 \langle \hat{n}_{\mathbf{k}\sigma} \rangle - 1) G^{|0\rangle\langle\beta_\sigma|}_{|\alpha_\sigma\rangle\langle 0|}(\tau,t) - F^{|0\rangle\langle\beta_\sigma|}_{|\alpha_\sigma\rangle\langle 0|}(\tau,t) \right] e^{i \int_t^\tau \epsilon_{\mathbf{k}}(x) dx} \right\}, \tag{3}$$

where the following Green-Keldysh functions [31] were introduced:

$$G^{|0\rangle\langle\beta_\sigma|}_{|\alpha_\sigma\rangle\langle 0|}(t,t') = i\theta(t'-t) \langle \{ |\alpha_\sigma\rangle \langle 0|_{(t')}, |0\rangle \langle\beta_\sigma|_{(t)} \} \rangle, \tag{4}$$

$$F^{|0\rangle\langle\beta_\sigma|}_{|\alpha_\sigma\rangle\langle 0|}(t,t') = i \langle [ |\alpha_\sigma\rangle \langle 0|_{(t')}, |0\rangle \langle\beta_\sigma|_{(t)} ] \rangle. \tag{5}$$

In Eq. (3), $\langle \hat{n}_{\mathbf{k}\sigma} \rangle$ corresponds to the average occupation of the $\mathbf{k}$ state with spin $\sigma$, which is given by the Fermi function $f_<(\epsilon_{\mathbf{k}}) = 1/(1 + e^{(\epsilon_{\mathbf{k}} - E_F)/k_B T})$. In the scattering of $Ga^+$ ions, Eq. (3) is solved with the initial condition $\langle \hat{n}_{\alpha_\sigma}(t_0) \rangle = 0$ for each $|\alpha_\sigma\rangle$ configuration. Equation (3) is valid for the other two approximations with small changes. In the independent states approach, only one state is considered at a time, so $\beta = \alpha$ and the sum over $\beta$ is lost, while in the spinless approximation, the spin index is also dropped.

The functions $G^{|0\rangle\langle\beta_\sigma|}_{|\alpha_\sigma\rangle\langle 0|}(t,t')$ and $F^{|0\rangle\langle\beta_\sigma|}_{|\alpha_\sigma\rangle\langle 0|}(t,t')$ are calculated through the EOM method closed within a strict second order in the atom-band coupling term [26]. More details are given in the Appendix.

#### 2. Stationary

The analysis of the stationary case, which corresponds to the system in equilibrium, allows us to gain insight into the physics of the more complex and nonintuitive time-dependent process. In this case, the important quantity is the spectral density for each atom configuration, given by

$$\rho_{\alpha_\sigma}(\omega) = \frac{1}{\pi} \mathrm{Im} \left[ G^{|0\rangle\langle\alpha_\sigma|}_{|\alpha_\sigma\rangle\langle 0|}(\omega) \right]. \tag{6}$$

From the spectral density, we obtain the average occupation as

$$\langle \hat{n}_{\alpha_\sigma} \rangle = \int_{-\infty}^{\infty} d\omega f_<(\omega) \rho_{\alpha_\sigma}(\omega). \tag{7}$$

By Fourier transforming Eq. (A10) of the Appendix, we obtain the following system of coupled algebraic equations that determines the Green functions $G^{|0\rangle\langle\beta_\sigma|}_{|\alpha_\sigma\rangle\langle 0|}(\omega)$:

$$\left[(\omega-\epsilon_\beta-i\eta)-\Sigma^t_{\beta\sigma}(\omega)\right]G^{|0\rangle\langle\beta_\sigma|}_{|\alpha_\sigma\rangle\langle 0|}(\omega) - \sum_{\gamma\neq\beta}\Sigma^t_{\beta\gamma\sigma}(\omega)G^{|0\rangle\langle\gamma_\sigma|}_{|\alpha_\sigma\rangle\langle 0|}(\omega) = (\langle|\alpha_\sigma\rangle\langle\beta_\sigma|\rangle+\delta_{\alpha\beta}\langle|0\rangle\langle 0|\rangle)+\Sigma^c_{\alpha\beta\sigma}(\omega). \quad (8)$$

The expression of the self-energy $\Sigma^t_{\beta\sigma}(\omega)$ introduced in Eq. (8) can be written as the sum of three terms,

$$\Sigma^t_{\beta\sigma}(\omega)=\Sigma^0_{\beta\beta}(\omega)+\Sigma^<_{\beta\beta\bar{\sigma}}(\omega)+\sum_{\gamma\neq\beta,\sigma'}\Sigma^<_{\gamma\sigma',\beta}(\omega), \quad (9)$$

where

$$\Sigma^0_{\beta\gamma}(\omega)=\sum_{\mathbf{k}}\frac{V_{\beta\mathbf{k}}V_{\mathbf{k}\gamma}}{(\omega-\epsilon_{\mathbf{k}}-i\eta)}, \quad (10)$$

$$\Sigma^<_{\beta\gamma\sigma}(\omega)=\sum_{\mathbf{k}}\frac{V_{\beta\mathbf{k}}V_{\mathbf{k}\gamma}\langle\hat{n}_{\mathbf{k}\sigma}\rangle}{(\omega-\epsilon_{\mathbf{k}}-i\eta)}, \quad (11)$$

$$\Sigma^<_{\gamma\sigma,\beta}(\omega)=\sum_{\mathbf{k}}\frac{V_{\gamma\mathbf{k}}V_{\mathbf{k}\gamma}\langle\hat{n}_{\mathbf{k}\sigma}\rangle}{(\omega-\epsilon_{\mathbf{k}}-\epsilon_\beta+\epsilon_\gamma-i\eta)}. \quad (12)$$

$\Sigma^0_{\beta\beta}$ corresponds to the typical self-energy for noninteracting electrons. Then, for the spinless approximation, it is the only self-energy involved. In this special case, the Green function is given simply by

$$G^{|0\rangle\langle\alpha_\sigma|}_{|\alpha_\sigma\rangle\langle 0|}(\omega)=\frac{1}{\left[\omega-\epsilon_\alpha-\Sigma^0_{\alpha\alpha}(\omega)-i\eta\right]}. \quad (13)$$

Only the first and second terms of Eq. (9) contribute to the self-energy in the independent states approximation, while the three terms participate in the correlated states case. In both cases, i.e., independent states and correlated states, the hopping integrals are divided by $\sqrt{2}$ in order to take into account the spin state degeneracy.

The off-diagonal terms in Eq. (8), $\Sigma^t_{\beta\gamma\sigma}(\omega)$, are given by

$$\Sigma^t_{\beta\gamma\sigma}(\omega)=\Sigma^0_{\beta\gamma}(\omega)-\Sigma^<_{\beta\gamma\sigma}(\omega). \quad (14)$$

Finally, the last term on the right-hand side of Eq. (8), $\Sigma^c_{\alpha\beta\sigma}(\omega)$, is given by

$$\Sigma^c_{\alpha\beta\sigma}(\omega)=(1-\delta_{\alpha\beta})\sum_{\mathbf{k}}\frac{V_{\beta\mathbf{k}}\langle|\alpha_\sigma\rangle\langle 0|c_{\mathbf{k}\sigma}\rangle}{(\omega-\epsilon_{\mathbf{k}}-i\eta)} - \delta_{\alpha\beta}\sum_{\mathbf{k}}\frac{V_{\beta\mathbf{k}}\langle|\beta_{\bar{\sigma}}\rangle\langle 0|c_{\mathbf{k}\bar{\sigma}}\rangle}{(\omega-\epsilon_{\mathbf{k}}-i\eta)} - \delta_{\alpha\beta}\sum_{\gamma\neq\beta,\mathbf{k},\sigma'}\frac{V_{\gamma\mathbf{k}}\langle|\gamma_{\sigma'}\rangle\langle 0|c_{\mathbf{k}\sigma'}\rangle}{(\omega-\epsilon_{\mathbf{k}}-\epsilon_\beta+\epsilon_\gamma-i\eta)}. \quad (15)$$

In this expression, the terms such as $\langle|\alpha_\sigma\rangle\langle 0|c_{\mathbf{k}\sigma}\rangle$ are given by

$$\langle|\alpha_\sigma\rangle\langle 0|c_{\mathbf{k}\sigma}\rangle=\int_{-\infty}^{+\infty}d\omega f_<(\omega)\rho^c_{\alpha\mathbf{k}_\sigma}(\omega), \quad (16)$$

where

$$\rho^c_{\alpha\mathbf{k}_\sigma}(\omega)=\frac{1}{\pi}\,\mathrm{Im}\left(\sum_\beta\frac{V_{\mathbf{k}\beta}G^{|0\rangle\langle\beta_\sigma|}_{|\alpha_\sigma\rangle\langle 0|}(\omega)}{(\omega-\epsilon_{\mathbf{k}}-i\eta)}\right). \quad (17)$$

The three terms in Eq. (15) are involved in the correlated states approximation, while only the second term is involved in the independent states approach.

## III. RESULTS

### A. Broaden and shift of the atom energy levels

A broadened atom energy level well defined above the Fermi energy is expected to be empty, while when it is well defined below the Fermi energy, it is expected to be occupied. Based on these intuitive arguments, the first insight into the charge state of an atom in front of a surface is provided by the shift and width of its one-electron energy levels. The real and imaginary parts of the self-energy, given by Eq. (9), evaluated at the energy level $\epsilon_\beta$, provide an estimation of the shift and width of this level, respectively.

Both magnitudes, the shift and the width, require one to calculate the hybridization terms $V_{\alpha\mathbf{k}}$. By using the bond-pair model [22], which is based on the expansion of the $\mathbf{k}$-band states in the atomic orbitals centered at the atoms of the solid, these terms are expressed as

$$V_{\alpha\mathbf{k}}(\mathbf{R})=\sum_{i,r}c^{\mathbf{k}}_{ir}V_{\alpha ir}(\mathbf{R}-\mathbf{R}_r). \quad (18)$$

In the expression above, $V_{\alpha ir}(\mathbf{R}-\mathbf{R}_r)$ are the atomic coupling between the states $i$ of the atom at position $\mathbf{R}_r$ in the solid and the orbital $p_\alpha$ of the projectile at position $\mathbf{R}$ (the coordinate system is centered on the scatterer surface atom with the $z$ axis perpendicular to the surface). The atom-atom coupling terms $V_{\alpha ir}$ are calculated by including the two-electron interactions in a mean-field approximation and by using a symmetrically orthonormalized atomic basis set in the dimeric space [22]. The coefficients $c^{\mathbf{k}}_{ir}$ of Eq. (18) are related to the density matrix of the solid, defined as

$$\rho_{ijrs}(\epsilon)=\sum_{\mathbf{k}}\left(c^{\mathbf{k}}_{ir}\right)^*c^{\mathbf{k}}_{js}\delta(\epsilon-\epsilon_{\mathbf{k}}). \quad (19)$$

The density matrix, calculated with the FIREBALL code [32,33], corresponds to the Au(100) surface.

In the experiment, the scattering angle is 135°, and the $Ga^+$ ions impact at 45° and exit at 90° with respect to the surface. This geometry allows us to consider, for the calculation, in and out trajectories that are perpendicular to the surface, with in and out velocities equal to the normal components of the experimental ones. The experimental condition of large scattering angle allows us to take into account only the surface scatterer atom at $\mathbf{R}_r=(0,0,0)$ in Eq. (18). Due to the low velocity of the projectile, the charge state will be defined at the exit trajectory, far from the surface and without keeping memory of the incoming trajectory [2,19–21]. Then, no parallel velocity effects are expected in this case.

As previously discussed, the real part of the self-energy of Eq. (9) corresponds to the shift of the energy level, while the imaginary part corresponds to its width. It is worth writing

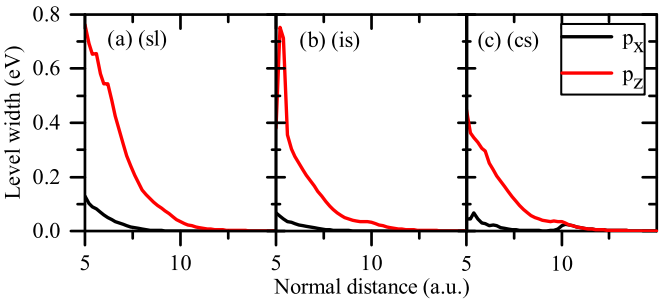


FIG. 2. Energy widths of the shifted energy levels for each approximation as a function of the distance to the surface.

explicitly the level width expressions in order to discuss the contribution from each term of Eq. (9). By replacing the expansion (18) in the expressions (10)–(12), and taking into account Eq. (19), the width $\Gamma$ of the $\epsilon_\beta$ level can be written as

$$\Gamma^t_{\beta\sigma}(\epsilon_\beta) = \Gamma^0_{\beta\beta}(\epsilon_\beta) + \Gamma^<_{\beta\beta\overline{\sigma}}(\epsilon_\beta) + \sum_{\gamma\neq\beta,\sigma'} \Gamma^<_{\gamma\sigma',\beta}(\epsilon_\beta), \quad (20)$$

where

$$\Gamma^0_{\beta\beta}(\epsilon_\beta) = \pi \sum_{i,j} \rho_{ij}(\epsilon_\beta) V_{\beta i} V_{j\beta}, \quad (21)$$

$$\Gamma^<_{\beta\beta\sigma}(\epsilon_\beta) = \pi f_<(\epsilon_\beta) \sum_{i,j} \rho_{ij}(\epsilon_\beta) V_{\beta i} V_{j\beta}, \quad (22)$$

$$\Gamma^<_{\gamma\sigma,\beta}(\epsilon_\beta) = \pi f_<(\epsilon_\gamma) \sum_{i,j} \rho_{ij}(\epsilon_\gamma) V_{\gamma i} V_{j\gamma}. \quad (23)$$

In Fig. 2, we show the widths of the shifted energy levels corresponding to each approximation as a function of the normal distance to the surface at $T = 300$ K. Strictly at $T = 0$ K, the contribution $\Gamma^<_{\beta\beta\overline{\sigma}}(\epsilon_\beta)$ comes into play when $\epsilon_\beta$ is below $E_F$. Therefore, if the levels are above $E_F$, the width in the independent states approach will be half of the corresponding spinless width, due to the renormalization of the hopping in the independent states case. Otherwise, both approximations, spinless and independent states, lead to the same level width. This analysis remains valid in the range of temperatures studied (up to 900 K). The larger widths of the $p_z$ state are due to the stronger coupling with the orbitals of the scatterer atom in the scattering geometry we are considering.

In Fig. 3, we show the shifted energy levels for the different approximations, assuming the energy widths shown in Fig. 2 as the energy uncertainty of the one-electron levels (the substrate temperature is fixed at 300 K). For the spinless and independent states approximations, $\epsilon_x$ remains near $E_F$, and it is slightly broadened and shifted. Under the correlated states approximation, the last term of Eq. (20), $\Gamma^<_{\gamma\sigma,\beta}(\epsilon_\beta)$, contributes to the total width when the remaining energy levels ($\gamma \neq \beta$) are below the $E_F$. This produces a broadening of the $\epsilon_x$ level while $\epsilon_z$ is below $E_F$, as can be seen in Fig. 2(c) and in the inset of Fig. 3(c). The shift of the $\epsilon_x$ level is due to the real part of $\Sigma^<_{z\sigma,x}(\epsilon_x)$ [see Eq. (9)]. The $\epsilon_z$ level is not affected by the presence of the other states because $\epsilon_x$ (and $\epsilon_y$) are above the Fermi level at distances where the couplings between the $p_x$ ($p_y$) orbital of the Ga atom and the orbitals of the surface atom are appreciable.

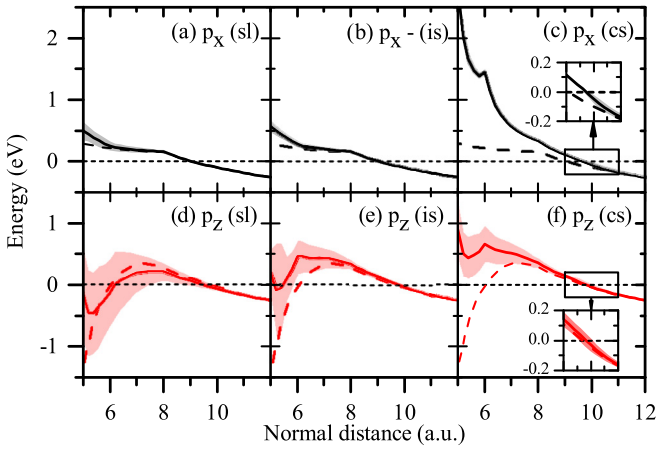


FIG. 3. Ga $4p$ states shifted energy levels (full line) with their corresponding widths (shaded) as a function of the normal projectile-surface distance. The results are shown for each approximation. The original levels are also depicted (dashed line).

With just a quick glance at Fig. 3, we expect a smaller occupation probability for the $|x_\sigma\rangle$ ($|y_\sigma\rangle$) configuration in the spinless approximation when contrasted to the independent states approach, at distances close to the surface. A negligible $\langle\hat{n}_{x_\sigma}\rangle$ ($\langle\hat{n}_{y_\sigma}\rangle$) is expected for the correlated states calculation. We can also infer from Fig. 3 that neglecting electron correlation leads to $\langle\hat{n}_{z_\sigma}\rangle$ occupations larger than that of independent states and correlated states, for which similar probability of occupations is expected.

We can see in the forthcoming section that the evolution of the occupation probabilities along the ion trajectory in both the stationary and dynamic situations is in line with this initial intuition.

### B. Evolution along the ion trajectory of the occupation probabilities

In the scattering process, the turning point is chosen to be 5 a.u. As in Refs. [9–11], the choice of the distance of closest approach was calculated as the sum of the atomic radii for Ga (2.45 a.u.) and Au (2.55 a.u.) [34]. The rationale of this assumption lies in the very low incoming velocity of the projectile. Nevertheless, even when higher turning points could be justified using different definitions of atomic radius (covalent radius, Van der Waals radius), the calculated neutral fractions slightly depend on the choice of distance of the closest approach for higher turning points within a reasonable range. The neutral fraction is calculated for an incoming ion energy of 2 keV, as in the experiment [4]. The energy-loss factor of the Ga-Au elastic collision with a 135° scattering angle, corresponding to 0.28, was used to calculate the exit velocity of the ion. In this section, the Au temperature is set at 300 K.

In Fig. 4, we show the probabilities of occupation along the ion trajectory for the three approximations: spinless (sl), independent states (is), and correlated states (cs), and the two situations analyzed: stationary [Fig. 4(a)] and dynamic [Fig. 4(b)]. In the independent states and correlated states approaches, the probabilities are summed over spin to make

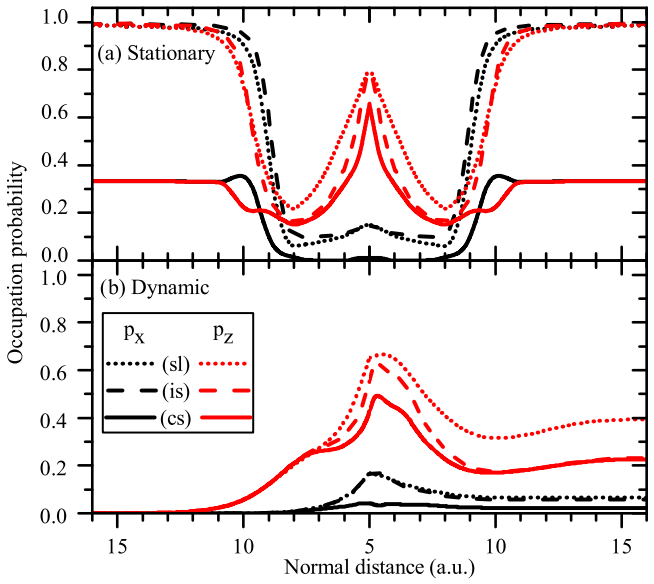


FIG. 4. (a) Equilibrium occupation probabilities in the stationary problem. (b) Evolution of the occupation probability along the incoming (left) and outgoing (right) trajectory. The probability of occupation of the $|x_\sigma\rangle$ and $|z_\sigma\rangle$ configurations is shown for the three approximations: spinless (sl), independent states (is), and correlated states (cs). The probabilities in the independent states and correlated states are summed over spin.

them comparable with the spinless case, that is, $\sum_\sigma \langle \hat{n}_{\alpha_\sigma}\rangle$ is shown for each $\alpha$. Far from the surface, the equilibrium values correspond to the configurations considered: 1 for the single spinless configuration; $\frac{1}{2}$ for the independent states case with spin fluctuation and independent states; and $\frac{1}{6}$ for the correlated states approximation where all six states are considered together. The dynamic evolution [Fig. 4(b)] shows the initial condition $\langle \hat{n}_{\alpha_\sigma}(t_0)\rangle = 0$.

As commented before, for the energy levels above $E_F$, the width in the spinless approximation is twice that of the independent states approach, while both approximations lead to the same width for levels below $E_F$. Then, the electron-loss process is less probable in the independent states approximation and therefore the probability of occupation must be larger, as it can be observed for $\langle \hat{n}_{x_\sigma}\rangle$ in Fig. 4(a).

The previous reasoning is strictly valid while the broadened levels are either well below or well above $E_F$ in both approximations, but is not so conclusive when they are relatively close to the Fermi energy. For instance, the larger width of $\epsilon_z$ in the spinless approximation when the atom level is above the Fermi energy makes it more possible that the electron-loss processes are far from the surface. In this form, we can understand the results of Fig. 4(a) for distances >9 a.u., which show that the equilibrium value of $\langle \hat{n}_{z_\sigma}\rangle$ in the spinless approximation is smaller than the corresponding one in the independent states case. Nevertheless, comparing Figs. 3(d) and 3(e), we see that the larger width which remains when the $\epsilon_z$ level is near $E_F$ in the spinless case allows capture processes near the surface. This gives place to a higher equilibrium value of $\langle \hat{n}_{z_\sigma}\rangle$ in this approximation for distances <9 a.u. [see Fig. 4(a)].

When the different neutral configurations are considered together, that is, in a correlated way, a strong shift of the $\epsilon_x$ ($\epsilon_y$) level occurs [see Fig. 3(c)], decreasing in this form the equilibrium average occupation $\langle \hat{n}_{x_\sigma}\rangle$ ($\langle \hat{n}_{y_\sigma}\rangle$) to negligible values close to the surface.

The correlated behavior of the different atom configurations, associated to the third terms of Eqs. (9) and (15), is clearly evidenced near 10 a.u., where the atom levels are crossing the Fermi level. The $\epsilon_z$ level crosses the $E_F$ farther from the surface than the $\epsilon_x$ level, and the appreciable width in this region [see inset of Fig. 3(f)] allows electron-loss processes while the $\epsilon_x$ ($\epsilon_y$) level remains below $E_F$. In this form, the occupations of the $|x_\sigma\rangle$ and $|y_\sigma\rangle$ configurations increase at the expense of the decreasing occupation of the $|z_\sigma\rangle$ one. The increase of the equilibrium value $\langle \hat{n}_{z_\sigma}\rangle$ when the other levels are above the Fermi energy is less important due to the negligible coupling of the $p_x$ ($p_y$) orbital with the surface.

The previous discussion also applies to the analysis of the dynamic evolution of $\langle \hat{n}_{\alpha_\sigma}\rangle$ presented in Fig. 4(b). For the $p_x$ orbital, the spinless and independent states approximations give similar results, while correlated states give place to a smaller value of $\langle \hat{n}_{x_\sigma}\rangle$. The spinless result for the occupation probability of the $|z_\sigma\rangle$ configuration is much greater than in the other cases, as a consequence of the larger width of the $\epsilon_z$ level, which remains close to the $E_F$ during almost the entire trajectory. For the other two approximations, the results differ near the surface and then converge to a similar value. The final value for the probability of occupation of the $|z_\sigma\rangle$ configuration is the largest, dominating the neutral fraction.

It is expected that the lower the ion velocity, the charge states of the projectile are defined at larger distances from the surface and become more similar to the equilibrium values. In this case, it is observed from Fig. 4 that the dynamic and stationary calculations give similar results in the outgoing part of the trajectory between 8 and 10 a.u., mainly in the correlated states case.

From this analysis, we can conclude that the spin-fluctuation statistic plus the correlated treatment of the different orbital configurations play an important role in the charge exchange between the Ga atom and the Au surface. Taking into account the spin statistics seems to be crucial in the case of the $|z_\sigma\rangle$ occupation, while the correlated treatment of all configurations has a higher impact on the occupations of $|x_\sigma\rangle$ and $|y_\sigma\rangle$.

### C. Temperature dependence

#### 1. Stationary

The ratio $r_\beta^c = \epsilon_\beta / \Gamma^0_{\beta\beta}(\epsilon_\beta)$ indicates the different correlation regimes in the infinite-U limit. Values of $|\epsilon_\beta| > \Gamma^0_{\beta\beta}(\epsilon_\beta)$ correspond to a Kondo regime when the energy level is below $E_F$ ($r_\beta^c < -1$) or to an empty orbital regime otherwise ($r_\beta^c > 1$). Intermediate values of $r_\beta^c$ correspond to a mixed-valence regime [17].

Taking into account the energy levels and their widths shown in Fig. 3, a mixed-valence regime evolving from a Kondo regime is expected far from the surface for all the configurations. It changes when the levels cross $E_F$: $\epsilon_x$ remains above $E_F$ and, in this case, a mixed valence evolving to an

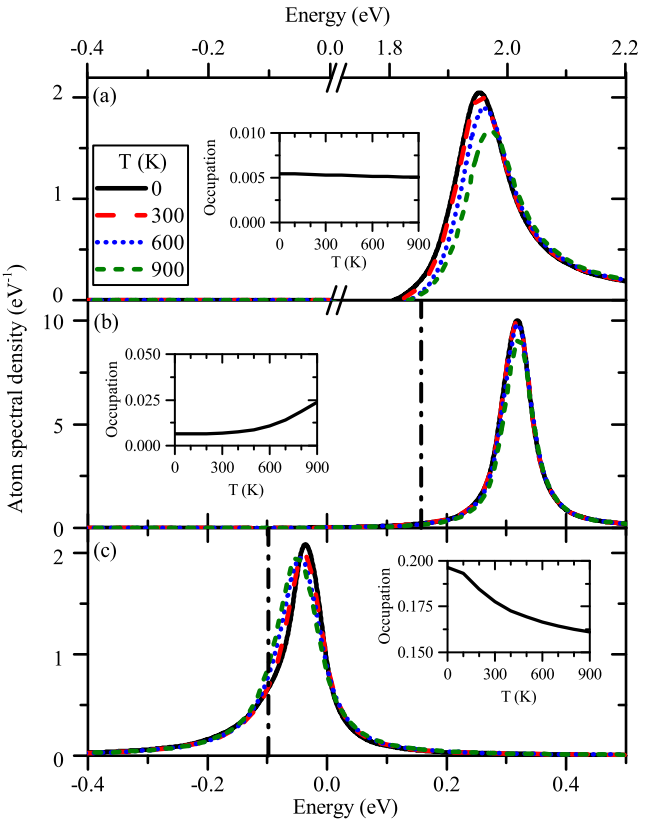


FIG. 5. Atom spectral density ($\rho_{\alpha_\sigma}$) for the $|x_\sigma\rangle$ configuration in the correlated states approximation at selected temperatures and atom-surface distances of (a) 5 a.u., (b) 8 a.u., and (c) 10 a.u. The dash-dotted lines indicate the position of the energy levels $\epsilon_\beta$; the resonance of the spectral density occurs in the shifted $\epsilon_\beta$ levels. The temperature dependence of the occupation probability is shown in the inset.

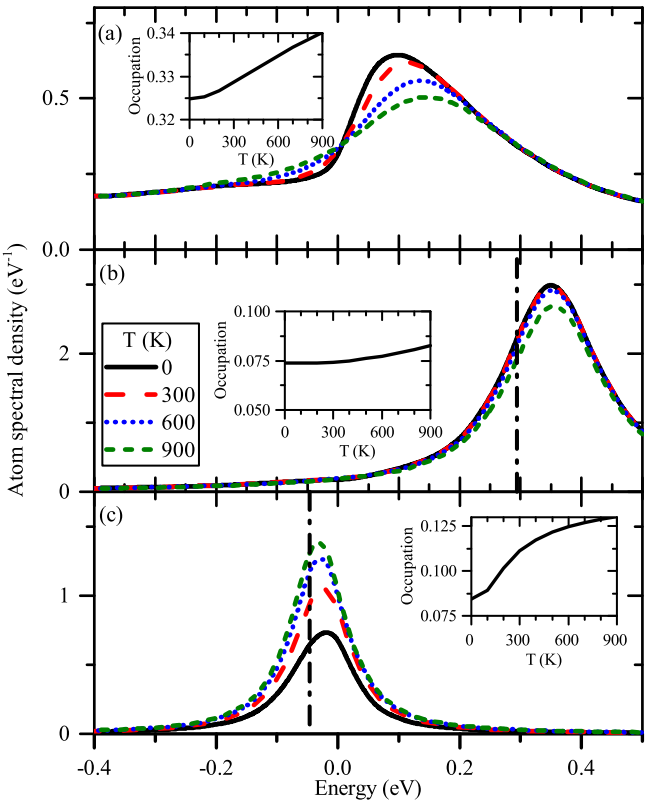


FIG. 6. Same as Fig. 5 for the $|z_\sigma\rangle$ configuration. Atom spectral density ($\rho_{\alpha_\sigma}$) in the correlated states approximation at selected temperatures and atom-surface distances of (a) 5 a.u., (b) 8 a.u., and (c) 10 a.u.. The dash-dotted lines indicate the position of the energy levels $\epsilon_\beta$. The temperature dependence of the occupation probability is shown in the inset.

empty orbital regime is expected, while the proximity of $\epsilon_z$ to $E_F$ suggests a better-defined mixed-valence regime for the $p_z$ orbital.

Figures 5 and 6 show the temperature dependence of the spectral densities [Eq. (6)] for the correlated states approximation. Depending on the distance to the surface, we observe either a decreasing occupation with temperature, indicating a mixed-valence regime evolving from a Kondo one, or an increasing occupation with temperature, indicating a mixed-valence regime evolving to an empty orbital. The $|x_\sigma\rangle$ ($|y_\sigma\rangle$) configuration responds to a mixed-valence regime evolving from a Kondo one for large distances and to an empty orbital regime for distances close to the surface. For the $|z_\sigma\rangle$ configuration, the mixed-valence regime prevails for practically all the range of distances where the interaction is non-null. In this form, all the configurations respond to a mixed-valence regime evolving from a Kondo regime as the atom approaches the surface.

It is worth noting the peculiar behavior of the spectral density of the $|z_\sigma\rangle$ configuration at 10 a.u. [Fig. 6(c)]. In this case, an increment of the occupation probability with temperature is observed while the $\epsilon_z$ level remains below the Fermi energy, a situation in which the opposite behavior is expected. This fact can be best understood by means of Fig. 7, which shows the temperature dependence of the occupation probabilities in the correlated states and independent states approaches. The correlation between the different configurations introduces a nontrivial dependence on temperature in the zone where the energy levels cross the Fermi energy. In this zone (around 10 a.u.), the occupation of the $|x_\sigma\rangle$ ($|y_\sigma\rangle$) configuration increases at the expense of the $|z_\sigma\rangle$ one, and shows an opposite dependence on temperature: $\langle\hat{n}_{x_\sigma}\rangle$ ($\langle\hat{n}_{y_\sigma}\rangle$) decreases with temperature, while $\langle\hat{n}_{z_\sigma}\rangle$ increases [see Fig. 7(a)]. As previously outlined, this behavior can also be observed from the spectral densities at 10 a.u. shown in Figs. 5(c) and 6(c), which are in correspondence with a mixed-valence regime evolving from a Kondo one in the case of the $|x_\sigma\rangle$ ($|y_\sigma\rangle$) configuration, and a more defined mixed valence in the case of the $|z_\sigma\rangle$ one. This peculiar behavior is not observed in the case of considering only the spin-fluctuation statistic, which is the approximation of independent states *(is)* shown in Fig. 7(b). In this case, we observe that the occupation probabilities decrease with temperature when the energy level is below the Fermi energy, while the opposite behavior is observed when the energy level is above the Fermi energy.

The increasing occupation of the $|z_\sigma\rangle$ configuration at close distances from the surface is explained by the proximity of the shifted $\epsilon_z$ level to the Fermi energy and its increasing width [see Fig. 3(f)]. This is also seen from the wide resonance of

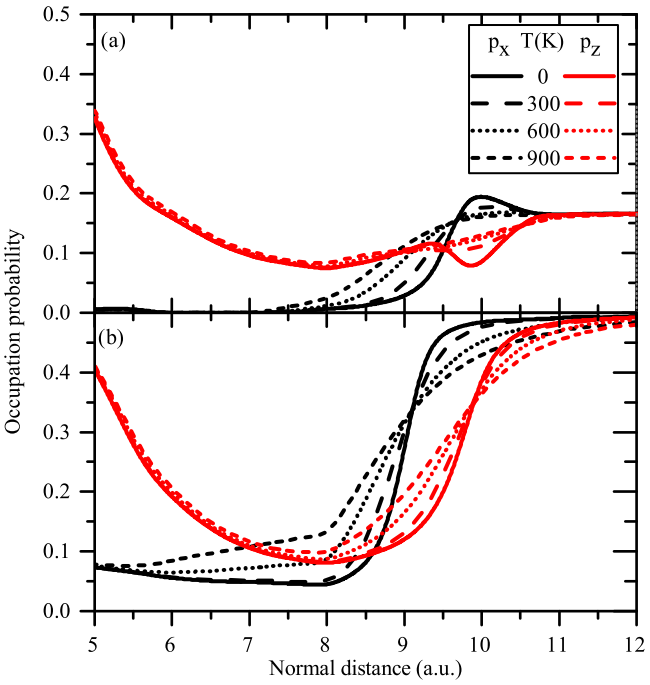


FIG. 7. (a) Equilibrium $\langle \hat{n}_{\alpha_\sigma} \rangle$ as a function of distance, in the correlated states approximation for the $|x_\sigma\rangle$ and $|z_\sigma\rangle$ configurations at several temperatures. (b) The same as in (a), but for the independent states case.

the spectral density shown in Fig. 6(a), which, on the other hand, is showing a well-defined mixed-valence regime at this distance.

### 2. *Dynamic*

The average occupation $\langle \hat{n}_{\alpha_\sigma} \rangle$ is the probability of having the neutral atom in the $|\alpha_\sigma\rangle$ state. Therefore, the neutral fraction $\langle n \rangle$ in the correlated states case is given by

$$\langle n \rangle_{cs} = \sum_{\alpha,\sigma} \langle \hat{n}_{\alpha_\sigma} \rangle \, . \tag{24}$$

In the other two approximations, i.e., spinless and independent states, where independent events are considered, the neutral fractions are given by

$$\langle n \rangle_{sl} = \sum_{\alpha} \langle \hat{n}_{\alpha} \rangle \prod_{\beta \neq \alpha} (1 - \langle \hat{n}_{\beta} \rangle) \tag{25}$$

in the spinless approximation, and by

$$\langle n \rangle_{is} = \sum_{\alpha,\sigma} \langle \hat{n}_{\alpha_\sigma} \rangle \prod_{\beta \neq \alpha} \left( 1 - \sum_{\sigma'} \langle \hat{n}_{\beta_{\sigma'}} \rangle \right) \tag{26}$$

in the independent states one.

Each term in the sum of either Eq. (25) or (26) gives the probability of occupation of one configuration remaining and the others empty. The total neutral fraction and the contributions from these terms [summed over spin in independent states and correlated states] are compared with the experimental results [4] in Fig. 8. The spinless approximation overestimates the measured neutral fraction and is not able to reproduce the measured temperature dependence. The experiment is

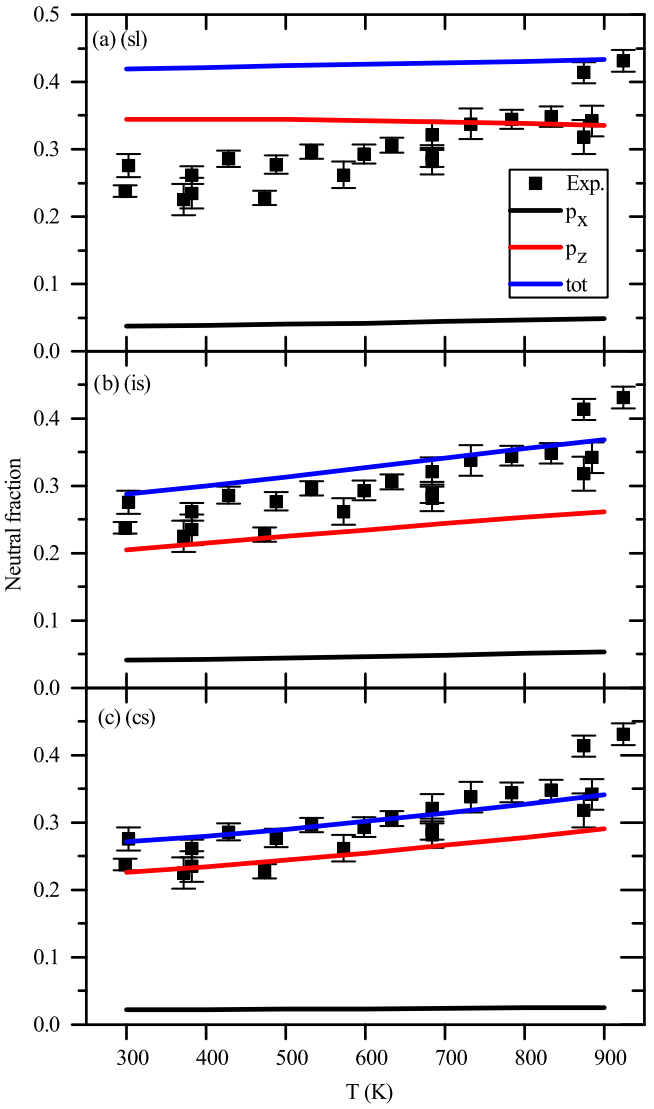


FIG. 8. Temperature dependence of the neutral fraction and the contributions of the $|x_\sigma\rangle$ and $|z_\sigma\rangle$ configurations, for each approximation. The contributions are summed over spin in the independent states (is) and correlated states (cs) cases. The experimental data [4] are also shown.

better reproduced by the correlated states calculation, which contemplates all possible configurations simultaneously. The main differences with the independent states approach are found in $\langle \hat{n}_{x_\sigma} \rangle$ and $\langle \hat{n}_{y_\sigma} \rangle$. These occupations are higher in the independent states approach, as we can see from Figs. 8(b) and 8(c). From Fig. 8, we can infer that not only the magnitude but also the temperature dependence of the measured neutral fraction is better reproduced when the correlation between the different neutralization channels is taken into account.

## D. Work-function dependence

Given the proximity of the projectile atom energy levels to the surface Fermi energy, the system is expected to be quite sensitive to the Au work function. In Fig. 9, the neutral fractions calculated under the correlated states approximation are shown as a function of temperature for several work

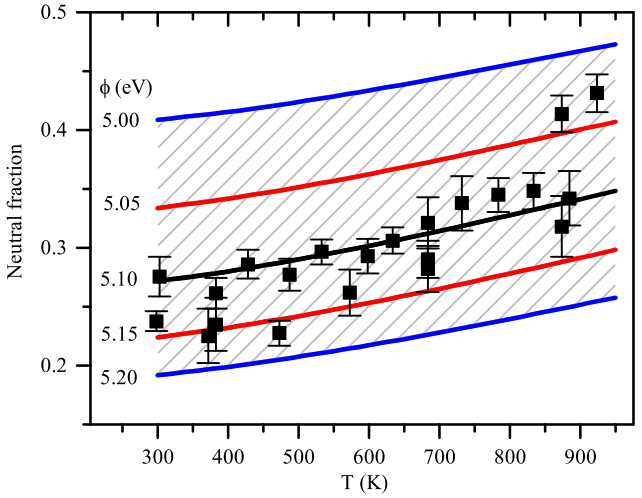


FIG. 9. Temperature dependence of the neutral fraction in the correlated states approximation at several work-function values. The experimental data [4] are also shown (squares).

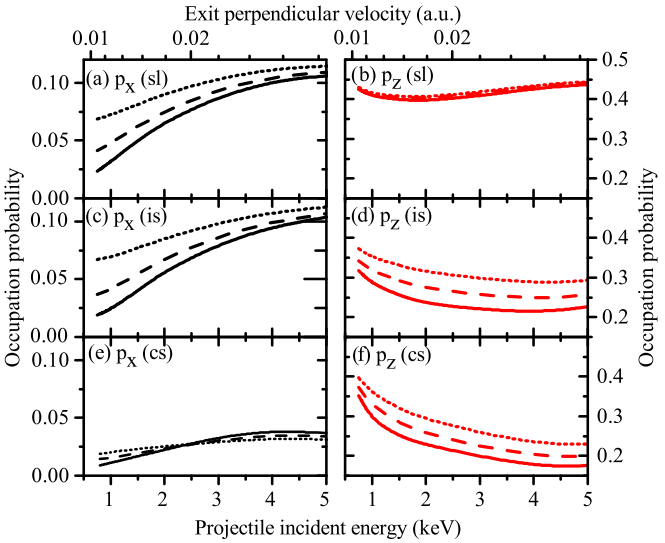


FIG. 10. Incident projectile energy dependence of $\langle \hat{n}_{x_\sigma} \rangle$ and $\langle \hat{n}_{z_\sigma} \rangle$ in the three approximations at 300 K (full line), 600 K (dashed line), and 900 K (dotted line). The cases independent states (is) and correlated states (cs) are summed over spin.

functions. We observe that all the experimental data are found within the band of theoretical values obtained by varying the work function up to the experimental uncertainty ($5.1 \pm 0.1$ eV) [4].

In the previously studied $Sr^+$/Au system [11], a nonmonotonous behavior of the work function with temperature was proposed to account for the measured temperature dependence of the neutral fraction [4]. Two possible causes for this dependence were proposed: sample heating, which involves thermal expansion of the crystal and thermal vibration of the atoms, and sample contamination under detection limits [11]. In light of our theoretical results for the $Ga^+$/Au system, we conclude that the nonmonotonous behavior of the gold work function with temperature is not intrinsic of the metal surface. Instead, it might be associated with Sr implantation.

### E. Projectile velocity dependence

As previously discussed, for very slow motion, the projectile charge state is defined at large distances from the surface and the memory of the interacting region closer to the surface is practically lost. As the velocity increases, it is expected that the effective distances for defining the projectile charge state become shorter. With these concepts in mind and the shifted and broadened levels shown in Fig. 3, we can understand quite well the velocity dependences of the occupations of the $|x_\sigma\rangle$ and $|y_\sigma\rangle$ configurations in the different approximations (Fig. 10). For the $|x_\sigma\rangle$ configuration, the electron-loss processes dominate over practically the whole effective interaction region. Then, for a longer interaction time (lower velocity), the occupation of this configuration is less probable. As we have noticed already, the spin-fluctuation statistics does not introduce practically any changes with respect to the spinless calculation for this configuration. Instead, for the $|z_\sigma\rangle$ configuration, the larger spinless level width [Figs. 3(d) and 3(e)] enables the electron-loss and capture processes as the velocity increases, leading to a minimum in the dependence of the occupation with the incident projectile energy. When the spin-fluctuation statistic is included, only electron-loss processes are enabled as the velocity increases (in the range of velocities of Fig. 10), and a decreasing occupation is obtained. This monotonous decreasing behavior with velocity is more pronounced in the correlated states approximation. We also can see that the dependence on the velocity of the $\langle \hat{n}_{x_\sigma} \rangle$ ($\langle \hat{n}_{y_\sigma} \rangle$) occupation is more affected by considering the correlated $p$ orbitals.

An increasing occupation with temperature is observed in the whole range of velocities analyzed, except for the correlated states $|x_\sigma\rangle$ ($|y_\sigma\rangle$) configuration, which presents an inversion of the dependence product of the interaction between states. As already noticed, for the $|z_\sigma\rangle$ configuration, the spin statistic introduces a stronger dependence on temperature compared with the spinless calculation.

The neutral fraction in the correlated states approach is shown as a function of temperature for several projectile incident energies ($E_P$) [Fig. 11(a)] and as a function of $E_P$ for three different temperatures [Fig. 11(b)]. In Fig. 11(a), we can observe that the temperature dependence is less pronounced for energies larger than 2 keV; this can be explained from the results shown in Figs. 10(e) and 10(f), which show that for $E_P > 3$ keV, the $\langle \hat{n}_{x_\sigma} \rangle$ ($\langle \hat{n}_{y_\sigma} \rangle$) occupation decreases with the temperature while the $\langle \hat{n}_{z_\sigma} \rangle$ occupation increases.

The dependence on the projectile energy shown in Fig. 11(b) for different temperatures is qualitatively very similar to that found when positive $Na^+$ ions are scattered by a Cu(001) surface [1]. In this system [1], the neutral fraction calculated by using a noninteracting electron model shows a minimum with an increasing dependence on the projectile exit perpendicular velocity, $v_P^e$, when $v_P^e > 0.01$ a.u. However, the experimental results show a slight dependence with $v_P^e$. In the present $Ga^+$/Au system, our spinless calculation is consistent with the theoretical findings reported in Ref. [1] [see Fig. 11(b)]. Nevertheless, when electronic correlation is introduced, we find a decreasing neutral fraction tending to a slight dependence on velocity for the analyzed values range.

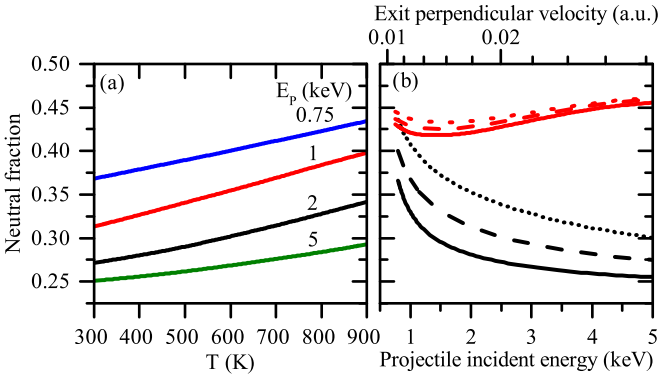


FIG. 11. (a) Temperature dependence of the neutral fraction in the correlated states approach for several incident projectile energies ($E_P$). (b) $E_P$ dependence of the neutral fraction in the correlated states (black) and spinless (red) approaches, for 300 K (full line), 600 K (dashed line), and 900 K (dotted line).

This effect is originated in the modified interaction with the band states due to the electronic repulsion, mainly associated to the new self-energy terms [Eq. (9)].

When the velocity increases, the time-energy uncertainty relation, proper for a dynamical scattering process ($\Delta E_u \approx v_P^e/2$ a.u.), starts to be comparable to the levels widths [25]. Within the energy uncertainty, the differences of the self-energies of the different approaches [Eq. (9)] become negligible. Therefore, the correlation evidenced in the system in the range of velocities studied is expected to be blurred in the limit of high velocities. Figure 12 shows the projectile energy dependence of the neutral fraction in each approach in a larger energy scale. It is worth noting that, as anticipated, results obtained from the three approaches converge to a single velocity dependence at incoming energies around 400 keV. Although an experiment at these velocities would probably be unfeasible, it is a sign of the consistency of the theoretical model applied.

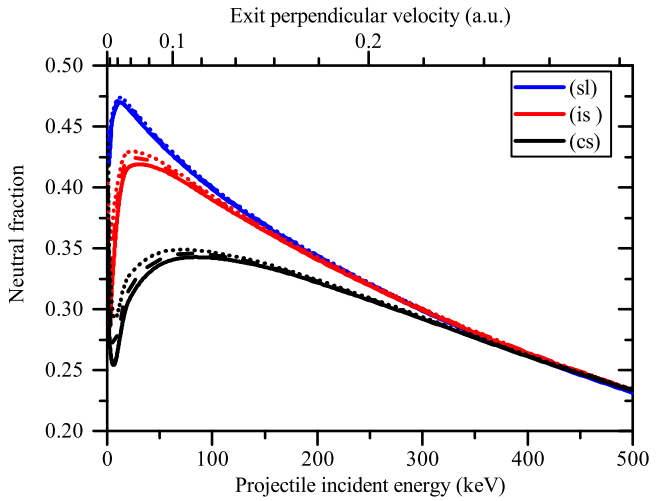


FIG. 12. Dependence of the neutral fraction for a large scale of projectile energies in the three approaches, for 300 K (full line), 600 K (dashed line), and 900 K (dotted line).

## IV. CONCLUSIONS

We proposed a theoretical model that successfully describes the experimental neutral fraction temperature dependence in low-energy collisions between $Ga^+$ and a gold surface. Six neutralization channels are considered simultaneously, consistent with the six spin and orbital components of an electron in a $p$ state.

We found that including the spin fluctuations (infinite correlation limit) is essential to describe the major contribution to the occupation ($p_z$ orbital), while the correlated treatment of all the involved atomic configurations mainly affects the minority occupations ($p_x$ and $p_y$ orbitals).

The analysis of the stationary interaction allows us to identify the different correlation regimes appearing in the adiabatic motion of the projectile along its trajectory. A mixed-valence regime prevails in the region where the ion final charge state is defined, suggesting an increasing valence occupation with the temperature as it is found experimentally.

The best agreement with experimental data was obtained when the electronic correlation was included in the model. Disregarding the electron correlation leads to a pronounced overestimation of the neutral fraction and to a practically nondependence with target temperature.

Unlike our previous study on $Sr^+$/Au, the calculated neutral fraction temperature dependence reproduces the measured data without the need to assume any gold work-function temperature dependence [11]. In light of these results, we conclude that in Ref. [11] the temperature dependence of the proposed work function is not intrinsic to the metal surface, but it might be linked to Sr implantation.

In addition, we show strong evidence suggesting that electron correlation effects might be essential to explain the velocity dependence of the neutral fraction experimentally found in alkaline positive ions scattered by metal surfaces [1].

Based on these findings, we conclude that the arguments based on the magnetic nature of the ion projectile to predict the importance of the electron correlation effects on the behavior of the neutral fraction with temperature are not valid. When dealing with closed-shell ions, the underlying reason is a change to a magnetic state (associated to an unpaired electron in the atom) when a resonant charge transfer process takes place.

The proximity between the surface Fermi level and the projectile one-electron energy levels is identified as a determinant factor in the final projectile charge state in low-energy collisions. Charge fluctuations involving energy levels close to the Fermi energy are more affected by electron-electron repulsion. The neutralization in these specific projectile/target systems will be particularly sensitive to temperature and work-function variations.

## ACKNOWLEDGMENTS

We gratefully acknowledge C. G. Pascual for providing us with the Au DOS. This work was supported by CONICET through PIP grants (No. 546) and U.N.L. through CAI + D grants (No. 50420150100014LI3).

## APPENDIX: DYNAMIC PROCESS EQUATIONS

In this Appendix, we present the calculation of the Green functions required to describe the time evolution of the occupation probabilities [Eq. (3)]. The Green functions, defined in Eqs. (4) and (5), are

$$G^{|0\rangle\langle\beta_\sigma|}_{|\alpha_\sigma\rangle\langle 0|}(t,t') = i\theta(t'-t)\langle\{|\alpha_\sigma\rangle\langle 0|_{(t')}, |0\rangle\langle\beta_\sigma|_{(t)}\}\rangle, \tag{A1}$$

$$F^{|0\rangle\langle\beta_\sigma|}_{|\alpha_\sigma\rangle\langle 0|}(t,t') = i\langle[|\alpha_\sigma\rangle\langle 0|_{(t')}, |0\rangle\langle\beta_\sigma|_{(t)}]\rangle. \tag{A2}$$

These Green functions are calculated by using the equations-of-motion method, which is based on the time evolution of an operator in the Heisenberg picture,

$$\frac{d\hat{O}}{dt} = -i[\hat{O},\hat{H}]. \tag{A3}$$

The derivative of both Green functions with respect to the first time variable $t$, maintaining the second one fixed, $t'$, leads to the following expressions:

$$\begin{aligned} i\frac{dG^{|0\rangle\langle\beta_\sigma|}_{|\alpha_\sigma\rangle\langle 0|}}{dt}(t,t') &= \delta(t'-t)(\langle|\alpha_\sigma\rangle\langle\beta_\sigma|\rangle_{(t')} + \delta_{\alpha\beta}\langle|0\rangle\langle 0|\rangle_{(t')}) + (E_\beta - E_0)G^{|0\rangle\langle\beta_\sigma|}_{|\alpha_\sigma\rangle\langle 0|}(t,t') \\ &\quad + \sum_{\mathbf{k}} V_{\beta\mathbf{k}} G^{|0\rangle\langle 0|c_{\mathbf{k}\sigma}}_{|\alpha_\sigma\rangle\langle 0|}(t,t') + \sum_{\mathbf{k},\gamma,\sigma'} V_{\gamma\mathbf{k}} G^{|\gamma_{\sigma'}\rangle\langle\beta_\sigma|c_{\mathbf{k}\sigma'}}_{|\alpha_\sigma\rangle\langle 0|}(t,t'), \end{aligned} \tag{A4}$$

$$i\frac{dF^{|0\rangle\langle\beta_\sigma|}_{|\alpha_\sigma\rangle\langle 0|}}{dt}(t,t') = (E_\beta - E_0)F^{|0\rangle\langle\beta_\sigma|}_{|\alpha_\sigma\rangle\langle 0|}(t,t') + \sum_{\mathbf{k}} V_{\beta\mathbf{k}} F^{|0\rangle\langle 0|c_{\mathbf{k}\sigma}}_{|\alpha_\sigma\rangle\langle 0|}(t,t') + \sum_{\mathbf{k},\gamma,\sigma'} V_{\gamma\mathbf{k}} F^{|\gamma_{\sigma'}\rangle\langle\beta_\sigma|c_{\mathbf{k}\sigma'}}_{|\alpha_\sigma\rangle\langle 0|}(t,t'). \tag{A5}$$

The notation for the new Green functions should be understood as in the definitions of Eqs. (A1) and (A2), for instance,

$$F^{|\gamma_{\sigma'}\rangle\langle\beta_\sigma|c_{\mathbf{k}\sigma'}}_{|\alpha_\sigma\rangle\langle 0|}(t,t') = i\langle[|\alpha_\sigma\rangle\langle 0|_{(t')}, |\gamma_{\sigma'}\rangle\langle\beta_\sigma|\, c_{\mathbf{k}\sigma'(t)}]\rangle. \tag{A6}$$

The following step is to perform the time derivative with respect to $t$ of the new Green functions appearing in Eqs. (A4) and (A5). The equations of motion are then closed by using mean-field approximations. For example,

$$F^{|0\rangle\langle\beta_\sigma|c^\dagger_{\mathbf{k}'\sigma'}c_{\mathbf{k}\sigma'}}_{|\alpha_\sigma\rangle\langle 0|}(t,t') = \delta_{\mathbf{k}'\mathbf{k}}\langle c^\dagger_{\mathbf{k}'\sigma'}c_{\mathbf{k}\sigma'}\rangle F^{|0\rangle\langle\beta_\sigma|}_{|\alpha_\sigma\rangle\langle 0|}(t,t'). \tag{A7}$$

In this form, after performing the phase transformations,

$$g^{|0\rangle\langle\beta_\sigma|}_{|\alpha_\sigma\rangle\langle 0|}(t,t') = G^{|0\rangle\langle\beta_\sigma|}_{|\alpha_\sigma\rangle\langle 0|}(t,t')e^{i\int_{t'}^{t}\epsilon_\beta dx}, \tag{A8}$$

$$f^{|0\rangle\langle\beta_\sigma|}_{|\alpha_\sigma\rangle\langle 0|}(t,t') = F^{|0\rangle\langle\beta_\sigma|}_{|\alpha_\sigma\rangle\langle 0|}(t,t')e^{i\int_{t'}^{t}\epsilon_\beta dx}, \tag{A9}$$

we arrive at

$$\begin{aligned} i\frac{dg^{|0\rangle\langle\beta_\sigma|}_{|\alpha_\sigma\rangle\langle 0|}}{dt}(t,t') &= \delta(t'-t)(\langle|\alpha_\sigma\rangle\langle\beta_\sigma|\rangle_{(t')} + \delta_{\alpha\beta}\langle|0\rangle\langle 0|\rangle_{(t')}) + \int_{t0}^{t'} d\tau\,\Sigma^t_{\beta\sigma}(\tau,t)g^{|0\rangle\langle\beta_\sigma|}_{|\alpha_\sigma\rangle\langle 0|}(\tau,t')e^{-i\int_t^\tau\epsilon_\beta dx} \\ &\quad + \sum_{\gamma\neq\beta}\int_{t0}^{t'} d\tau\,\Sigma^t_{\beta\gamma\sigma}(\tau,t)g^{|0\rangle\langle\gamma_\sigma|}_{|\alpha_\sigma\rangle\langle 0|}(\tau,t')e^{-i\int_{t'}^\tau\epsilon_\gamma dx}e^{-i\int_t^{t'}\epsilon_\beta dx} + \Sigma^c_{\alpha\beta\sigma}(t',t)e^{-i\int_t^{t'}\epsilon_\beta dx}, \end{aligned} \tag{A10}$$

$$\begin{aligned} i\frac{df^{|0\rangle\langle\beta_\sigma|}_{|\alpha_\sigma\rangle\langle 0|}}{dt}(t,t') &= \int_{t_0}^{t'} d\tau\big(\Sigma^{t(r)}_{\beta\sigma}(\tau,t)f^{|0\rangle\langle\beta_\sigma|}_{|\alpha_\sigma\rangle\langle 0|}(\tau,t') + \Omega^t_{\beta\sigma}(\tau,t)g^{|0\rangle\langle\beta_\sigma|}_{|\alpha_\sigma\rangle\langle 0|}(\tau,t')\big)e^{-i\int_t^\tau\epsilon_\beta dx} + \sum_{\gamma\neq\beta}\int_{t_0}^{t'} d\tau\big(\Sigma^{t(r)}_{\beta\gamma\sigma}(\tau,t)f^{|0\rangle\langle\gamma_\sigma|}_{|\alpha_\sigma\rangle\langle 0|}(\tau,t') \\ &\quad + \Omega^t_{\beta\gamma\sigma}(\tau,t)g^{|0\rangle\langle\gamma_\sigma|}_{|\alpha_\sigma\rangle\langle 0|}(\tau,t')\big)e^{-i\int_{t'}^\tau\epsilon_\gamma dx}e^{-i\int_t^{t'}\epsilon_\beta dx} + \Omega^c_{\alpha\beta\sigma}(t',t)e^{-i\int_t^{t'}\epsilon_\beta dx}. \end{aligned} \tag{A11}$$

The expressions of the different quantities introduced in Eq. (A10) are given by

$$\Sigma^t_{\beta\sigma}(\tau,t) = \Sigma^0_{\beta\beta}(\tau,t) + \Sigma^<_{\beta\beta\bar{\sigma}}(\tau,t) + \sum_{\gamma\neq\beta,\sigma'}\Sigma^<_{\gamma\sigma',\beta}(\tau,t), \tag{A12}$$

$$\Sigma^t_{\beta\gamma\sigma}(\tau,t) = \Sigma^0_{\beta\gamma}(\tau,t) - \Sigma^<_{\beta\gamma\sigma}(\tau,t), \tag{A13}$$

$$\Sigma^{c}_{\alpha\beta\sigma}(t',t) = i\theta(t'-t)(1-\delta_{\alpha\beta})\sum_{\mathbf{k}} V_{\beta\mathbf{k}}(t)\,\langle|\alpha_\sigma\rangle\,\langle 0|\,c_{\mathbf{k}\sigma}\rangle_{(t')}\,e^{i\int_t^{t'}\epsilon_{\mathbf{k}}dx}$$
$$- i\theta(t'-t)\delta_{\alpha\beta}\sum_{\mathbf{k}} V_{\beta\mathbf{k}}(t)\,\langle|\beta_{\bar\sigma}\rangle\,\langle 0|\,c_{\mathbf{k}\bar\sigma}\rangle_{(t')}\,e^{i\int_t^{t'}\epsilon_{\mathbf{k}}dx}$$
$$- i\theta(t'-t)\delta_{\alpha\beta}\sum_{\mathbf{k},\gamma\neq\beta,\sigma'} V_{\gamma\mathbf{k}}(t)\,\langle|\gamma_{\sigma'}\rangle\,\langle 0|\,c_{\mathbf{k}\sigma'}\rangle_{(t')}\,e^{i\int_t^{t'}(\epsilon_{\mathbf{k}}+\epsilon_\beta-\epsilon_\gamma)dx}, \tag{A14}$$

where

$$\Sigma^{0}_{\beta\gamma}(\tau,t) = i\theta(\tau-t)\sum_{\mathbf{k}} V_{\beta\mathbf{k}}(t)V_{\mathbf{k}\gamma}(\tau)e^{i\int_t^{\tau}\epsilon_{\mathbf{k}}dx}, \tag{A15}$$
$$\Sigma^{<}_{\beta\gamma\sigma}(\tau,t) = i\theta(\tau-t)\sum_{\mathbf{k}} V_{\beta\mathbf{k}}(t)V_{\mathbf{k}\gamma}(\tau)\,\langle n_{\mathbf{k}\sigma}\rangle\,e^{i\int_t^{\tau}\epsilon_{\mathbf{k}}dx}, \tag{A16}$$
$$\Sigma^{<}_{\gamma\sigma,\beta}(\tau,t) = i\theta(\tau-t)\sum_{\mathbf{k}} V_{\gamma\mathbf{k}}(t)V_{\mathbf{k}\gamma}(\tau)\,\langle n_{\mathbf{k}\sigma}\rangle\,e^{i\int_t^{\tau}(\epsilon_{\mathbf{k}}+\epsilon_\beta-\epsilon_\gamma)dx}. \tag{A17}$$

The retarded self-energies introduced in Eq. (A11) are related to Eqs. (A12) and (A13) through the relations

$$\Sigma^{t(r)}_{\beta\sigma}(\tau,t) = \left[\Sigma^{t}_{\beta\sigma}(t,\tau)\right]^*, \tag{A18}$$
$$\Sigma^{t(r)}_{\beta\gamma\sigma}(\tau,t) = \left[\Sigma^{t}_{\gamma\beta\sigma}(t,\tau)\right]^*. \tag{A19}$$

The rest of the quantities introduced in Eq. (A11) are given by

$$\Omega^{t}_{\beta\sigma}(\tau,t) = \Omega^{0}_{\beta\beta,\sigma}(\tau,t) + \Omega^{<}_{\beta\beta\bar\sigma,\sigma}(\tau,t) + \sum_{\gamma\neq\beta,\sigma'}\Omega^{<}_{\gamma\sigma',\beta,\sigma}(\tau,t), \tag{A20}$$
$$\Omega^{t}_{\beta\gamma\sigma}(\tau,t) = \Omega^{0}_{\beta\gamma,\sigma}(\tau,t) - \Omega^{<}_{\beta\gamma\sigma,\sigma}(\tau,t), \tag{A21}$$
$$\Omega^{c}_{\alpha\beta\sigma}(t',t) = i(1-\delta_{\alpha\beta})\sum_{\mathbf{k}}(2\,\langle n_{\mathbf{k}\sigma}\rangle - 1)V_{\beta\mathbf{k}}(t)\,\langle|\alpha_\sigma\rangle\,\langle 0|\,c_{\mathbf{k}\sigma}\rangle_{(t')}\,e^{i\int_t^{t'}\epsilon_{\mathbf{k}}dx}$$
$$- i\delta_{\alpha\beta}\sum_{\mathbf{k}}(2\,\langle n_{\mathbf{k}\sigma}\rangle - 1)V_{\beta\mathbf{k}}(t)\,\langle|\beta_{\bar\sigma}\rangle\,\langle 0|\,c_{\mathbf{k}\bar\sigma}\rangle_{(t')}\,e^{i\int_t^{t'}\epsilon_{\mathbf{k}}dx}$$
$$- i\delta_{\alpha\beta}\sum_{\mathbf{k},\gamma\neq\beta,\sigma'}(2\,\langle n_{\mathbf{k}\sigma}\rangle - 1)V_{\gamma\mathbf{k}}(t)\,\langle|\gamma_{\sigma'}\rangle\,\langle 0|\,c_{\mathbf{k}\sigma'}\rangle_{(t')}\,e^{i\int_t^{t'}(\epsilon_{\mathbf{k}}+\epsilon_\beta-\epsilon_\gamma)dx}, \tag{A22}$$

where

$$\Omega^{0}_{\beta\gamma,\sigma}(\tau,t) = i\sum_{\mathbf{k}}(2\,\langle n_{\mathbf{k}\sigma}\rangle - 1)V_{\beta\mathbf{k}}(t)V_{\mathbf{k}\gamma}(\tau)e^{i\int_t^{\tau}\epsilon_{\mathbf{k}}dx}, \tag{A23}$$
$$\Omega^{<}_{\beta\gamma\sigma',\sigma}(\tau,t) = i\sum_{\mathbf{k}}(2\,\langle n_{\mathbf{k}\sigma}\rangle - 1)V_{\beta\mathbf{k}}(t)V_{\mathbf{k}k\gamma}(\tau)\,\langle n_{\mathbf{k}\sigma'}\rangle\,e^{i\int_t^{\tau}\epsilon_{\mathbf{k}}dx}, \tag{A24}$$
$$\Omega^{<}_{\gamma\sigma',\beta,\sigma}(\tau,t) = i\sum_{\mathbf{k}}(2\,\langle n_{\mathbf{k}\sigma}\rangle - 1)V_{\gamma\mathbf{k}}(t)V_{\mathbf{k}\gamma}(\tau)\,\langle n_{\mathbf{k}\sigma'}\rangle\,e^{i\int_t^{\tau}(\epsilon_{\mathbf{k}}+\epsilon_\beta-\epsilon_\gamma)dx}. \tag{A25}$$

The atom-band crossed terms $\langle|\alpha_\sigma\rangle\,\langle 0|\,c_{\mathbf{k}\sigma}\rangle_{(t)}$ appearing in Eqs. (A14) and (A22) are given by

$$\langle|\alpha_\sigma\rangle\,\langle 0|\,c_{\mathbf{k}\sigma}\rangle_{(t)} = \frac{1}{2}\sum_{\beta}\int_{t_0}^{t} d\tau\, V_{\mathbf{k}\beta}(\tau)\Big((2\,\langle\hat n_{\mathbf{k}\sigma}\rangle - 1)g^{|0\rangle\langle\beta_\sigma|}_{|\alpha_\sigma\rangle\langle 0|}(\tau,t) - f^{|0\rangle\langle\beta_\sigma|}_{|\alpha_\sigma\rangle\langle 0|}(\tau,t)\Big)e^{i\int_t^{\tau}(\epsilon_{\mathbf{k}}-\epsilon_\beta)dx}. \tag{A26}$$

The integrals in $\mathbf{k}$ space, involved in all of the expressions above, are replaced by integrals over the band energies by considering the linear combination of atomic orbitals (LCAO) expansion of the coupling parameters, given by Eq. (18). In this form, we have, for any function $h(\epsilon_{\mathbf{k}},\ldots)$,

$$\sum_{\mathbf{k}} V_{\alpha\mathbf{k}}(t)V_{\mathbf{k}\beta}(\tau)h(\epsilon_{\mathbf{k}},\ldots) = \sum_{i,j,r,s} V_{\alpha ir}(t)[V_{\beta js}(\tau)]^*\int_{-\infty}^{\infty}\rho_{ijrs}(\epsilon)h(\epsilon,\ldots)d\epsilon, \tag{A27}$$

where $\rho_{ijrs}(\epsilon)$ is the density matrix of the solid, given by Eq. (19).

A description of the numerical details for solving a system of coupled integrodifferential equations such as Eqs. (A10) and (A11) is given in Ref. [35]. Here we outline the main steps. Equation (A10) is integrated for each fixed time $t'$, from $t = t'$ to

$t = t_0$ (initial time corresponding to the atom-surface systems without interaction) by considering the boundary condition for $t = t'$,

$$g^{|0\rangle\langle\beta_\sigma|}_{|\alpha_\sigma\rangle\langle 0|}(t \to t', t') = i(\langle|\alpha_\sigma\rangle\ \langle\beta_\sigma|\rangle_{(t')} + \delta_{\alpha\beta}\ \langle|0\rangle\ \langle 0|\rangle_{(t')}). \tag{A28}$$

Then, we integrate Eq. (A11) from $t = t_0$ to $t = t'$ by using the boundary condition based on the noninteracting atom-surface system at $t = t_0$ and the initial atom electronic configuration $\langle \hat{n}_{\alpha_\sigma}(t_0)\rangle = 0$,

$$f^{|0\rangle\langle\alpha_\sigma|}_{|\alpha_\sigma\rangle\langle 0|}(t_0, t') = -g^{|0\rangle\langle\alpha_\sigma|}_{|\alpha_\sigma\rangle\langle 0|}(t_0, t'). \tag{A29}$$

Equation (3) is then integrated to obtain the occupations and the calculation continues by incrementing the fixed value of $t'$ in such a way that it runs over the complete time interval from $t_0$ to $t_{\max}$ (the time value for which the atom-surface interaction becomes negligible along the outgoing trajectory).


[1] C. E. Sosolik, J. R. Hampton, A. C. Lavery, B. H. Cooper, and J. B. Marston, Phys. Rev. Lett. **90**, 013201 (2003).

[2] A. V. Onufriev and J. B. Marston, Phys. Rev. B **53**, 13340 (1996).

[3] J. Merino and J. B. Marston, Phys. Rev. B **58**, 6982 (1998).

[4] X. He and J. A. Yarmoff, Phys. Rev. Lett. **105**, 176806 (2010).

[5] X. He and J. A. Yarmoff, Nucl. Instr. Methods Phys. Res. Sect. B **269**, 1195 (2011).

[6] D. C. Langreth and P. Nordlander, Phys. Rev. B **43**, 2541 (1991).

[7] H. Shao, D. C. Langreth, and P. Nordlander, Phys. Rev. B **49**, 13929 (1994).

[8] H. Shao, P. Nordlander, and D. C. Langreth, Phys. Rev. Lett. **77**, 948 (1996).

[9] M. Pamperin, F. X. Bronold, and H. Fehske, Phys. Rev. B **91**, 035440 (2015).

[10] M. Pamperin, F. X. Bronold, and H. Fehske, Phys. Scr. **T165**, 014008 (2015).

[11] F. Bonetto, C. Gonzalez, and E. C. Goldberg, Phys. Rev. B **93**, 195439 (2016).

[12] N. P. Wang, E. A. García, R. Monreal, F. Flores, E. C. Goldberg, H. H. Brongersma, and P. Bauer, Phys. Rev. A **64**, 012901 (2001).

[13] S. Rund, D. Primetzhofer, S. Markin, D. Goebl, and P. Bauer, NIMB **269**, 1171 (2011).

[14] A. Iglesias-García, E. A. García, and E. C. Goldberg, Phys. Rev. B **87**, 075434 (2013).

[15] A. Iglesias-García, E. A. García, and E. C. Goldberg, Phys. Rev. B **90**, 195416 (2014).

[16] K. K. Kouache, Nucl. Inst. Methods Phys. Res. **382**, 11 (2016).

[17] A. C. Hewson, *The Kondo Problem to Heavy Fermions* (Cambridge University Press, Cambridge, 1993).

[18] P. W. Anderson, Phys. Rev. **124**, 41 (1961).

[19] M. Plihal and D. C. Langreth, Phys. Rev. B **58**, 2191 (1998).

[20] C. Meyer, F. Bonetto, R. Vidal, E. A. García, C. Gonzalez, J. Ferrón, and E. C. Goldberg, Phys. Rev. A **86**, 032901 (2012).

[21] F. Bonetto, M. A. Romero, E. A. García, R. A. Vidal, J. Ferrón, and E. C. Goldberg, Phys. Rev. B **78**, 075422 (2008).

[22] P. G. Bolcatto, E. C. Goldberg, and M. C. G. Passeggi, Phys. Rev. B **58**, 5007 (1998).

[23] F. J. Bonetto, E. A. García, C. González, and E. C. Goldberg, J. Phys. Chem. C **118**, 8359 (2014).

[24] A. Iglesias-García, F. Bonetto, R. Vidal, J. Ferrón, and E. C. Goldberg, Phys. Rev. A **89**, 042702 (2014).

[25] F. J. Bonetto, M. A. Romero, A. Iglesias-García, R. A. Vidal, and E. C. Goldberg, J. Phys. Chem. C **119**, 3124 (2015).

[26] E. C. Goldberg, F. Flores, and R. C. Monreal, Phys. Rev. B **71**, 035112 (2005).

[27] S. Huzinaga, J. Andzelm, M. Klobukowsky, E. Radzio-Andzelm, Y. Sakai, and H. Tatewaki, *Gaussian Basis Set for Molecular Calculations* (Elsevier, Amsterdam, 1984).

[28] S. Huzinaga, J. Chem. Phys. **42**, 1293 (1965).

[29] M. Frisch, G. Trucks, H. Schlegel, G. Scuseria, M. Robb, J. Cheeseman, V. Zakrzewski, J. Montgomery Jr, R. Stratmann, J. Burant *et al.*, computer code GAUSSIAN98, *rev. A.7* (Gaussian Inc., Pittsburgh, PA, 1998).

[30] M. A. Romero, F. Flores, and E. C. Goldberg, Phys. Rev. B **80**, 235427 (2009).

[31] L. V. Keldysh, J. Exp. Theor. Phys. **20**, 1018 (1965).

[32] J. P. Lewis, K. R. Glaesemann, G. A. Voth, J. Fritsch, A. A. Demkov, J. Ortega, and O. F. Sankey, Phys. Rev. B **64**, 195103 (2001).

[33] P. Jelinek, H. Wang, J. P. Lewis, O. F. Sankey, and J. Ortega, Phys. Rev. B **71**, 235101 (2005).

[34] J. C. Slater, J. Chem. Phys. **41**, 3199 (1964).

[35] H. Aoki, N. Tsuji, M. Eckstein, M. Kollar, T. Oka, and P. Werner, Rev. Mod. Phys. **86**, 779 (2014).